

FrPolad: Frequency-Rectified Point Latent Diffusion for Point Cloud Generation

Chenliang Zhou¹, Fangcheng Zhong¹, Param Hanji¹, Zhilin Guo¹,
Kyle Fogarty¹, Alejandro Sztrajman¹, Hongyun Gao¹, Cengiz Oztireli¹

Department of Computer Science and Technology,
Cambridge, University of Cambridge, UK

Abstract. We propose *FrPolad: frequency-rectified point latent diffusion*, a point cloud generation pipeline integrating a variational autoencoder (VAE) with a denoising diffusion probabilistic model (DDPM) for the latent distribution. FrPolad simultaneously achieves high quality, diversity, and flexibility in point cloud cardinality for generation tasks while maintaining high computational efficiency. The improvement in generation quality and diversity is achieved through (1) a novel frequency rectification via spherical harmonics designed to retain high-frequency content while learning the point cloud distribution; and (2) a latent DDPM to learn the regularized yet complex latent distribution. In addition, FrPolad supports variable point cloud cardinality by formulating the sampling of points as conditional distributions over a latent shape distribution. Finally, the low-dimensional latent space encoded by the VAE contributes to FrPolad’s fast and scalable sampling. Our quantitative and qualitative results demonstrate FrPolad’s state-of-the-art performance in terms of quality, diversity, and computational efficiency. Project page: <https://chenliang-zhou.github.io/FrPolad/>.

Keywords: Point cloud generation · Computer vision · Frequency analysis

1 Introduction

Point clouds are a widely-used 3D representation with extensive applications in 3D content creation and reconstruction [20, 22, 27, 38, 38, 46, 94, 98, 103]. Automated 3D content creation using point clouds has been extensively explored in recent studies through the adoption of generative methods, such as autoencoders [39, 97], adversarial training [38, 99], flow-based models [37, 44], and denoising diffusion probabilistic models (DDPM) [57, 89]. However, addressing the intricate task of learning the distributions of point clouds while simultaneously attaining exceptional sample *quality*, *diversity*, and *computational efficiency* poses a substantial challenge. For example, variational autoencoders (VAEs) [42] and generative adversarial networks (GANs) [25] tend to produce noisy or blurry outcomes [16, 19, 35], possibly attributed to the *loss of high-frequency information* [16, 19, 47] caused by the *spectral bias* [40, 58] (also see Sec. 2). Excessive

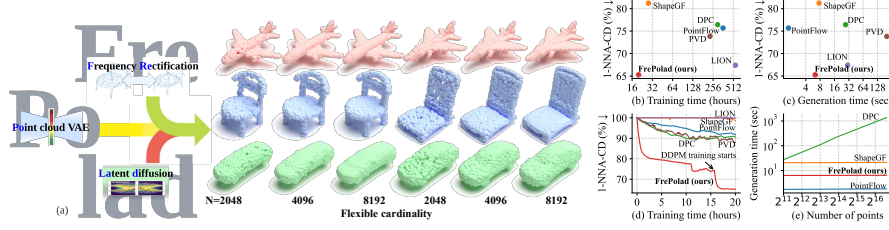


Fig. 1: (a) FrePolad combines novel frequency rectification with a point cloud VAE and a DDPM-based prior to generate point clouds with superior quality, diversity, and flexibility in cardinality. Plots show on the right (b) training and (c) generation costs *vs.* final validation score measured by 1-NNA-CD (↓), (d) learning curves for the first 20 hours of training, and (e) generation cost for synthesizing different numbers of points

emphasis on generation fidelity, such as through the deployment of excessively deep networks, can lead to reduced diversity and even mode collapse [52, 100]. VAEs also struggle with the *prior hole problem* [79, 87, 88] when employing over-simplified Gaussian priors [10]. While normalizing flows [75] and DDPMs [30, 83] have emerged as powerful generative models, they face challenges in learning high-dimensional distributions, particularly for point clouds. A key issue with both classes of models is the necessity for the latent distribution to match the dimensionality of the target. Thus, despite their exceptional sample quality and diversity in various domains [14, 43, 61, 66, 84, 93], directly applying these models to point cloud generation results in only moderate success [57, 96, 103].

Generating point clouds with flexible cardinality (varying number of points) is also a critical, yet often overlooked feature in recent works. Prior works with fixed cardinalities [1, 22] often fail to incorporate the inherent property of permutation invariance in point clouds. The methods that are trained with heuristic loss functions such as Chamfer distance (CD) or earth mover’s distance (EMD) can also distort the probabilistic interpretation of VAEs [96]. Furthermore, the flexibility in cardinality is crucial for tasks involving non-uniform datasets, such as those from LiDAR scans [24, 80]. Networks with unrestricted cardinality readily scale for tasks with unspecified output point count requirements, avoiding the significant computational overhead associated with retraining fixed-cardinality models, while demonstrating superior quality compared to post-processing the point cloud with upsampling (see Sec. 5.4).

To simultaneously address the outlined challenges, we propose a novel generative framework, *FrePolad: frequency-rectified point latent diffusion*. FrePolad integrates a point cloud VAE with a latent DDPM modeling its latent distribution. Given that VAEs typically have access to a low-dimensional latent space, leveraging DDPMs to learn the VAE-encoded latent distributions enhances complex distribution modeling [64, 89], preserves high-frequency contents [77, 88], and reduces computational demands (Sec. 5.3). Furthermore, harnessing insights from spherical harmonic analysis, we introduce a novel *frequency rectification* technique for training the point cloud VAE to further strengthen the preservation of

high-frequency contents, thereby significantly boosting the sample fidelity and diversity (Sec. 5.3). Finally, FrePolad supports a variable number of points in the training set via a permutation-invariant set encoder [68, 69]. By formulating the sampling of points as a conditional distribution over a latent shape distribution, *i.e.*, a *distribution of distributions*, FrePolad enables arbitrary cardinality in point cloud generation. Our extensive evaluation of FrePolad on the ShapeNet dataset [7] demonstrates its state-of-the-art performance in terms of generation quality and diversity, while incurring the least computational expense (Fig. 1).

Our contributions are summarized as follows:

- A novel point cloud generative network realized through a variational autoencoder (VAE) with a prior distribution based on a denoising diffusion probabilistic model (DDPM) (Sec. 4);
- An novel *frequency rectification* technique designed to promote the preservation of high-frequency details during VAE training (Secs. 4.1 and 4.2);
- A comprehensive demonstration of FrePolad’s state-of-the-art performance in terms of quality, diversity, and computational efficiency through extensive experiments and analysis (Sec. 5).

2 Related works

Denoising diffusion probabilistic models Recent advancements in denoising diffusion probabilistic models (DDPMs) [30, 83] have demonstrated remarkable performance in various domains, including image synthesis [4, 14, 30, 73, 77], density estimation [41], and speech synthesis [8, 33, 54]. Nonetheless, DDPMs are known to lack a low-dimensional, interpretable space [64] and to be time-inefficient during generation. Given that variational autoencoders (VAEs) typically have access to a low-dimensional latent space, researchers have explored the potential of DDPMs to model VAE-encoded latent distributions across various modalities, including images [73, 82], music [59], videos [2, 28, 102], and point cloud generation [89, 96]. Along this direction, our work further probes the efficacy of this paired framework in the domain of point cloud generation.

Point cloud generation A multitude of studies have delved into point cloud generation within various generative frameworks, including auto-regressive autoencoding [22, 39, 42, 76, 97], adversarial generation [1, 25, 38, 48, 55, 81, 99], flow-based models [15, 37, 43, 44, 96], and, recently, DDPMs [55, 57, 60, 63, 89, 94, 94, 103]. Recently, LION [89] proposes the VAE framework based on PVCNNs [55] with a hierarchical latent space modeled by two DDPMs. Nevertheless, while a hierarchical latent space can be effective in capturing complex distributions [31, 67, 73], an overly intricate network topology and multilayered latent codes – where a single layer exceeds the original point cloud’s dimensionality – may lead to challenges such as overfitting [65], lack of interpretability [101], and excessive computational cost during both training and sampling.

On the other hand, most works in point cloud generation primarily target at modeling the data distribution of point clouds within $\mathbb{R}^{3 \times N}$ with a fixed number

N of points [1, 22]. The limitation of such approach has been discussed in Sec. 1 and in many other works [57, 96]. In contrast, contemporary research has explored a different approach conceptualizing point clouds as probabilistic distributions in \mathbb{R}^3 , leading to the modeling of a *distribution of distributions* [5, 44, 57, 85, 96, 97].

Frequency analysis in VAE Variational autoencoders (VAEs) [42] are probabilistic generative networks modeling the probability distributions of datasets. A pervasive challenge associated with VAEs is their tendency to attenuate high-frequency data [18], often resulting in blurry or low-resolution samples [16, 19, 32, 35, 47]. This degradation becomes even more pronounced at higher compression rates [53]. Such loss of high-frequency details can be attributed to the intrinsic *spectral bias* in general neural network layers [40, 58, 71, 86] and/or to the upsampling modules in VAEs [6, 17, 92] during reconstruction or generation.

Various VAE architectures have been proposed to promote data reconstruction in the frequency domain [23, 34, 95]. Predominantly, these architectures utilize Fourier features [72] or positional encoding [58, 90] to preserve high-frequency details [13, 23, 34, 53]. Yet, a limitation exists: they lack generalizability to point cloud data since Fourier analysis requires data with a well-defined grid structure – such as 2D grids in images or 3D grids in voxels. Drawing inspiration from [62], in Secs. 4.1 and 4.2, we adopt spherical harmonic analysis for frequency information extraction from point clouds.

3 Background

3.1 Variational Autoencoder

We use a VAE [42] as our latent distribution model as it provides access to a low-dimensional latent space and has been successfully applied to generate point clouds [50, 51, 91]. VAEs are probabilistic generative models that can model a probability distribution of a given dataset \mathcal{X} . A VAE consists of an encoder $q_\psi(\mathbf{z}|\mathbf{X})$ and a decoder $p_\xi(\mathbf{X}|\mathbf{z})$ parametrized by ψ and ξ , respectively. Assuming that the latent codes $\mathbf{z} \in \mathbb{R}^{D_z}$ follow a prior distribution $p(\mathbf{z})$, the encoder and decoder are jointly trained to maximize the *evidence lowerbound (ELBO)*:

$$\mathcal{L}_{\text{ELBO}}(\psi, \xi; \mathbf{X}) := \mathbb{E}_{q_\psi(\mathbf{z}|\mathbf{X})} [\log p_\xi(\mathbf{X}|\mathbf{z})] - \mathcal{D}_{\text{KL}}(q_\psi(\mathbf{z}|\mathbf{X}), p(\mathbf{z})), \quad (1)$$

where \mathcal{D}_{KL} is the Kullback-Leibler divergence between the two distributions [12].

3.2 Denoising Diffusion Probabilistic Model

Our generative framework leverages a denoising diffusion probabilistic model (DDPM) [30, 83] to model the complexity of the VAE latent space. Given a data sample $\mathbf{z} \sim p(\mathbf{z})$, at each time step $t = 1, 2, \dots, T$, DDPMs gradually transform $\mathbf{z} = \mathbf{z}_0$ into \mathbf{z}_T by adding noise in a Markovian diffusion process according to a predetermined variance schedule $\{\beta_t\}_t$. If T is sufficiently large (1000 steps in practice), $p(\mathbf{z}_T)$ will approach the standard Gaussian distribution $\mathcal{N}(0, I)$.

Furthermore, since all transition kernels of the diffusion process are Gaussian: $p(\mathbf{z}_t | \mathbf{z}_{t-1}) \sim \mathcal{N}(\mathbf{z}_t; \sqrt{1 - \beta_t} \mathbf{z}_{t-1}, \beta_t I)$, $\forall t$, samples from the intermediate distributions can be directly generated in a single step:

$$\mathbf{z}_t = \alpha_t \mathbf{z}_0 + \gamma_t \boldsymbol{\epsilon}, \quad (2)$$

where $\alpha_t := \prod_{i=1}^t \sqrt{1 - \beta_i}$, $\gamma_t := \sqrt{1 - \alpha_t^2}$, and $\boldsymbol{\epsilon} \sim \mathcal{N}(0, I)$. The objective is to train a parametric model $\boldsymbol{\epsilon}_\zeta(\mathbf{z}_t, t)$ by minimizing the score matching objective,

$$\mathcal{L}_{\text{DDPM}}(\boldsymbol{\zeta}) := \mathbb{E}_{p(\mathbf{z}_0), t \sim \mathcal{U}(1, T), \boldsymbol{\epsilon} \sim \mathcal{N}(0, I)} [\|\boldsymbol{\epsilon} - \boldsymbol{\epsilon}_\zeta(\mathbf{z}_t, t)\|_2^2], \quad (3)$$

where $\mathcal{U}(1, T)$ is the uniform distribution on $\{1, 2, \dots, T\}$.

During inference, the network allows sampling through an iterative procedure since the learned distribution can be factorized as

$$p_\zeta(\mathbf{z}) = p(\mathbf{z}_T) p_\zeta(\mathbf{z} | \mathbf{z}_T) = p(\mathbf{z}_T) \prod_{t=1}^T p_\zeta(\mathbf{z}_{t-1} | \mathbf{z}_t) \quad (4)$$

for $p(\mathbf{z}_T) := \mathcal{N}(0, I)$.

For a more detailed derivation, please refer to Sec. 6 in the supplementary.

3.3 Spherical Harmonics

The spherical harmonics [11] are a set of base functions $Y_{l,m} : S^2 \rightarrow \mathbb{C}$ defined on a unit sphere S^2 indexed by the degree $l \geq 0$ and the order m ($-l \leq m \leq l$). They form an orthonormal basis for square-intergrable functions defined on the unit sphere $L^2(S^2)$ [71]; *i.e.*, every such function f can be represented as

$$f(\theta, \varphi) = \sum_{l=0}^{\infty} \sum_{m=-l}^l c_{l,m} Y_{l,m}(\theta, \varphi). \quad (5)$$

where the coefficients $c_{l,m}$ can be calculated by

$$c_{l,m} = \int_0^{2\pi} \int_0^\pi f(\theta, \varphi) \overline{Y_{l,m}(\theta, \varphi)} \sin(\theta) d\theta d\varphi. \quad (6)$$

Similar to Fourier analysis [21], spherical harmonics cast spatial data into the spectral domain, allowing the extraction of frequency-specific information: coefficients $c_{l,m}$ with a higher degree measure the intensity of the original data in a higher-frequency domain. Please refer to Sec. 6 in the supplementary for more details about spherical harmonics.

4 Formulation

We aim to learn a generative model to synthesize point clouds $\mathbf{X} \in \mathbb{R}^{3 \times N_x}$ consisting of N_x points with a distribution $p(\mathbf{X})$. Following [96], we treat each

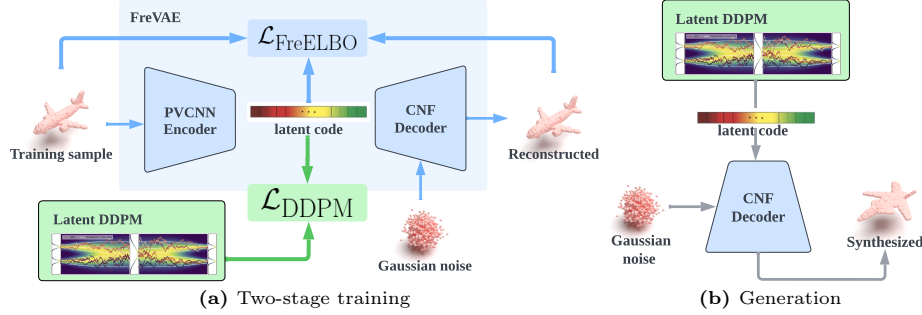


Fig. 2: FrePolad is architected as a point cloud VAE, with an embedded latent DDPM to represent the latent distribution. (a) Two-stage training: in the first stage (blue), the VAE is optimized to maximize the FreELBO Eq. (15) with a standard Gaussian prior; in the second stage (green), while fixing the VAE, the latent DDPM is trained to model the latent distribution. (b) Generation: conditioned on a shape latent sampled from the DDPM, the CNF decoder transforms a Gaussian noise input into a synthesized shape.

\mathbf{X} as a distribution $p(\mathbf{x}|\mathbf{z})$ over its points $\mathbf{x} \in \mathbb{R}^3$, conditioned on the latent vector $\mathbf{z} \sim p(\mathbf{z})$ of the underlying shape. Note that once $p(\mathbf{x}|\mathbf{z})$ is properly learned, the cardinality of the point cloud is unrestricted as one can sample an arbitrary number of points from this distribution.

Figure 2 presents an overview of our generative model, *frequency-rectified point latent diffusion (FrePolad)*. FrePolad amalgamates a point cloud VAE that models $p(\mathbf{x}|\mathbf{z})$ with a DDPM modeling its latent distribution $p(\mathbf{z})$. Synthesis is performed by sampling a shape latent from the DDPM which is subsequently decoded into a point cloud. To train the VAE, we leverage spherical harmonics and extract frequency information from point clouds (Sec. 4.1). Then, we formulate a novel frequency rectification module that encourages the reconstruction of high-frequency regions (Sec. 4.2). In addition, we employ a latent DDPM for enhanced expressiveness, continuous preservation of high-frequency contents, and reduced dimensionality. Collectively, we harmonize these components for our model, FrePolad, to facilitate point cloud generation (Sec. 4.4).

4.1 Frequency Extraction via Spherical Harmonics

In order to extract frequency information with spherical harmonics (Eq. (5)), we seek to represent the underlying surface of a point cloud $\mathbf{X} \in \mathbb{R}^{3 \times N_x}$ consisting of N_x points by a continuous function on the unit sphere, *i.e.*, $f_{\mathbf{X}}(\theta, \varphi)$. Note that, with this representation, we assume the surface is a *star domain*. We start by expressing each 3D point in spherical coordinates $\mathbf{x}_i = (r_i, \theta_i, \varphi_i)$. Next, we construct $f_{\mathbf{X}}$ by anchoring each point $\mathbf{x}_i \in \mathbf{X}$ to its radius r_i and interpolating

in the rest of the domain:

$$f_{\mathbf{X}}(\theta, \varphi) := \begin{cases} r & (\theta, \varphi, r) \in \mathbf{X} \\ \sum_{\substack{(\theta_i, \varphi_i) \\ \in \mathcal{H}_{\mathbf{X}}(\theta, \varphi)}} w_i(\theta, \varphi) r_i & \text{otherwise} \end{cases}, \quad (7)$$

where $\mathcal{H}_{\mathbf{X}}(\theta, \varphi)$ is the set of k closest neighbors (θ_i, φ_i) of (θ, φ) with $(r_i, \theta_i, \varphi_i) \in \mathbf{X}$ for some r_i , determined according to the following distance function d ,

$$d_{\text{sphere}}((\theta, \varphi), (\theta', \varphi')) := \sqrt{2 - 2[\sin \theta \sin \theta' \cos(\varphi - \varphi') + \cos \theta \cos \theta']}, \quad (8)$$

and $w_i(\theta, \varphi)$ are the weights.

Since closer points should have larger weights, $\{w_i(\theta, \varphi)\}_i$ should be a decreasing sequence on $d_{\text{sphere}}((\theta, \varphi), (\theta_i, \varphi_i))$. A suitable candidate is the normalized Gaussian function with standard deviation σ_{KNN} :

$$w'_i(\theta, \varphi) := e^{-\frac{d_{\text{sphere}}^2((\theta, \varphi), (\theta_i, \varphi_i))}{2\sigma_{\text{KNN}}^2}} \text{ and } w'_{ij} := \frac{w'_{ij}}{\sum_j w'_{ij}}. \quad (9)$$

Defining $f_{\mathbf{X}}$ in this way presents limitations for point clouds with non-star-domain shapes. Specifically, at some values of θ and ϕ , there may exist multiple points from semantically different regions of the point cloud. Nevertheless, we found this formulation to be computationally efficient and empirically superior to more complex alternatives (see the ablation study in Sec. 5.3 for more details).

After representing \mathbf{X} by $f_{\mathbf{X}}$, we extract frequency information by computing its spherical harmonic coefficients $c_{l,m}^{\mathbf{X}}$ via Eq. (6); these coefficients reveal the original point cloud \mathbf{X} in frequency domains. We show a point cloud and its representative function in spherical and frequency domains in Fig. 3 (first row).

4.2 Frequency-Rectified VAE

As discussed earlier, VAEs suffer from losing high-frequency data, and existing remedies do not generalize well to point clouds [16, 19, 32, 35, 47]. To mitigate this problem, we utilize the frequency information extracted in Sec. 4.1 and propose *frequency rectification* in training the VAE that promotes the preservation of high-frequency information.

We first define a frequency-rectified distance $d_{\text{Fre}}(\mathbf{X}, \mathbf{X}')$ between two point clouds \mathbf{X} and \mathbf{X}' :

$$d_{\text{Fre}}(\mathbf{X}, \mathbf{X}') := \sum_{l=0}^{\infty} \sum_{m=-l}^l r_l \left\| c_{l,m}^{\mathbf{X}} - c_{l,m}^{\mathbf{X}'} \right\|_2^2, \quad (10)$$

where $\{r_l\}_l$ is a sequence of increasing *frequency rectifiers* that weight higher-degree spherical harmonic coefficients more. In practice, we restrict the infinite sum and evaluate the first $L+1$ terms. The frequency rectifiers are given by the Gaussian function:

$$r_l := e^{-\frac{(L-l)^2}{2\sigma_{\text{Fre}}^2}}. \quad (11)$$

A frequency rectified loss between encoder and decoder distributions can be obtained by taking the expectation over point clouds \mathbf{X}' learned by the VAE:

$$\mathcal{L}_{\text{Fre}}(\psi, \xi; \mathbf{X}) := \mathbb{E}_{\mathbf{z} \sim q_\psi(\mathbf{z}|\mathbf{X}), \mathbf{X}' \sim p_\xi(\mathbf{X}'|\mathbf{z})} [d_{\text{Fre}}(\mathbf{X}, \mathbf{X}')] \quad (12)$$

In order to encourage the reconstruction of high-frequency regions, we introduce a constraint while maximizing the ELBO (Eq. (1)):

$$\begin{aligned} & \max_{\psi, \xi} \mathbb{E}_{\mathbf{X} \sim p(\mathbf{X})} [\mathcal{L}_{\text{ELBO}}(\psi, \xi; \mathbf{X})] \\ & \text{s.t. } \mathbb{E}_{\mathbf{X} \sim p(\mathbf{X})} [\mathcal{L}_{\text{Fre}}(\psi, \xi; \mathbf{X})] < \delta, \end{aligned} \quad (13)$$

where $\delta > 0$ controls the strength of this constraint. Leveraging Karush–Kuhn–Tucker (KKT) methods [36, 45], we can re-write the above constrained optimization problem (13) as a Lagrange function whose optimal point is a global maximum over the domain of (ψ, ξ) :

$$\mathcal{F}(\psi, \xi, \eta; \mathbf{X}) := \mathcal{L}_{\text{ELBO}}(\psi, \xi; \mathbf{X}) - \eta (\mathcal{L}_{\text{Fre}}(\psi, \xi; \mathbf{X}) - \delta), \quad (14)$$

where η is the KKT multiplier. Since $\delta > 0$, we obtain a lower-bound on the ELBO:

$$\begin{aligned} \mathcal{F}(\psi, \xi, \eta; \mathbf{X}) & \geq \mathcal{L}_{\text{ELBO}}(\psi, \xi; \mathbf{X}) - \eta \mathcal{L}_{\text{Fre}}(\psi, \xi; \mathbf{X}) \\ & =: \mathcal{L}_{\text{FreELBO}}(\psi, \xi, \eta; \mathbf{X}). \end{aligned} \quad (15)$$

Our encoder and decoder networks are trained by maximizing the novel *frequency-rectified evidence lowerbound (FreELBO)* $\mathcal{L}_{\text{FreELBO}}$. The hyperparameter η trades-off reconstruction quality between the spatial and spectral domains. When $\eta = 0$, the training objective is the same as the original ELBO Eq. (1); when $\eta > 0$, inaccuracies in reconstructing high-frequency regions are penalized.

An example of a frequency-rectified point cloud is shown in Fig. 3. We observe that after frequency rectification, points shift to more complex or less smooth regions in the point clouds, corresponding to higher frequency areas. Additionally, in the frequency domain, we see that as lower-frequency features (with lower degrees) are decayed by the rectifiers Eq. (11), the relative significance of higher-frequency features amplifies. Consequently, our VAE prioritizes the reconstruction in these regions.

4.3 DDPM-Based Prior

Although it is possible to sample shape latents from a simple Gaussian prior for generation, evidence suggests that such a restricted prior cannot accurately capture complex encoder distributions, $q_\psi(\mathbf{z}|\mathbf{X})$. This is known as the *prior hole problem* [79, 87, 88], and tends to curtail the performance of VAEs [10], resulting in the poor reconstructions in our ablation study (see Sec. 5.3). To address this, we employ a DDPM to model the VAE’s latent distribution [77]. The DDPM is trained on the latents \mathbf{z} directly sampled from $q_\psi(\mathbf{z}|\mathbf{X})$. Since the original prior is insufficient, the DDPM learns a more expressive distribution

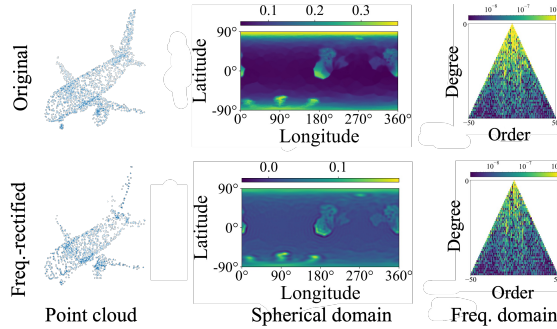


Fig. 3: A point cloud before and after frequency rectification and its representative function in spherical and frequency domains. Frequency rectification shifts points to more complex, less smooth regions and increases the relative importance of higher-frequency features, where VAEs can give more attention during reconstruction. Note that the frequency rectified point cloud in the second row is only for visualization; our framework does not explicitly generate such a point cloud during training.

$p_\zeta(\mathbf{z})$, better matches the true latent distribution $p(\mathbf{z})$, and functions as the VAE’s prior. Combining latent DDPM with a VAE-based model helps achieve a near-ideal equilibrium between minimizing complexity and ensuring perceptual fidelity [77, 88]. Crucially, the high-frequency details maintained by frequency rectification during encoding stage remain undisturbed. Additionally, learning the distribution of shape latents instead of point clouds significantly reduces the training and sampling cost (see Tab. 3) due to the reduced dimensionality. This enables scalable generation of much denser point clouds (see Fig. 5).

4.4 FrePolad

With all the building blocks, we present our new generative model for point cloud generation: *FrePolad: frequency-rectified point latent diffusion*. The overall structure of our framework is presented in Fig. 2.

Components The VAE encoder $q_\psi(\mathbf{z}|\mathbf{X})$ is a Point-Voxel CNN (PVCNN) [55, 103] parametrized by ψ . PVCNNs efficiently combine the point-based processing of PointNets [68, 69] with the strong spatial inductive bias of convolutions. Our encoder accommodates point clouds of variable cardinalities and is permutation-invariant.

In order to support flexible cardinality while synthesizing point clouds, we interpret each point cloud \mathbf{X} as a distribution $p(\mathbf{x}|\mathbf{z})$ of its constituent points conditioned on the shape latent \mathbf{z} . Assuming independence among the points in a point cloud, we model the decoder distribution as

$$p_\xi(\mathbf{X}|\mathbf{z}) := \prod_{\mathbf{x} \in \mathbf{X}} p_\xi(\mathbf{x}|\mathbf{z}). \quad (16)$$

The decoder is implemented using a conditional continuous normalizing flow (CNF) [9, 26, 75]. Here, a sampled point \mathbf{x} is the result of transforming some initial point $\mathbf{x}(0) \sim p(\mathbf{x}(0)) := \mathcal{N}(0, I)$, conditioned on the shape latent \mathbf{z} . The invertible nature of CNFs offers a high degree of interpretability and also allows the exact computation of data likelihood $p(\mathbf{x}|\mathbf{z})$ by moving the transformed points back to the prior distribution. For more details, please see Sec. 6 in the supplementary.

The latent DDPM $p_\zeta(\mathbf{z})$ is parametrized by ζ , realized through a U-Net backbone [78] following [77].

Training Following common practice [5, 19, 74, 77], we perform a two-stage training. In the first stage, we train the VAE network by maximizing the FreELBO Eq. (15) with the prior $p(\mathbf{z}) := \mathcal{N}(0, I)$. In the second stage, we freeze the VAE network and train the DDPM on the latent vectors sampled from the encoder $q_\psi(\mathbf{z}|\mathbf{X})$ by minimizing the objective function Eq. (3).

Generation During generation, new point clouds of arbitrary cardinality can be generated by first sampling a shape latent \mathbf{z} from the DDPM $p_\zeta(\mathbf{z})$ following Eq. (4) and then sampling the decoder $p_\zeta(\mathbf{X}|\mathbf{z})$ following Eq. (16): Formally, the generation process of FrePolad is defined by

$$p_{\xi, \zeta}(\mathbf{X}) := p_\zeta(\mathbf{z})p_\xi(\mathbf{X}|\mathbf{z}). \quad (17)$$

5 Experiments

In this section, we provide experiments demonstrating FrePolad’s performance in point cloud generation. Please refer to Sec. 6 in the supplementary for training and hyperparameter details.

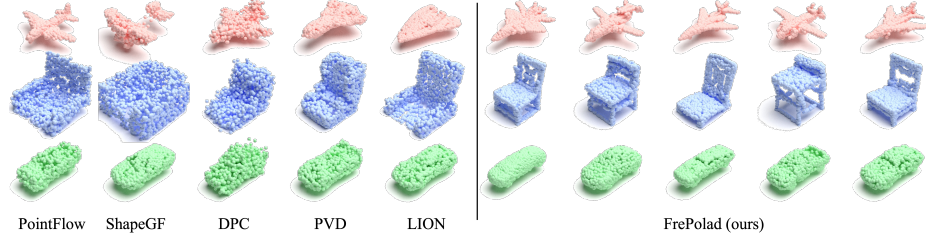


Fig. 4: Generation with 2048 points for airplane, chair, and car classes. Samples generated by FrePolad have better fidelity and diversity.

5.1 Dataset

To benchmark FrePolad against existing methods, we employ ShapeNet [7], a widely used dataset for 3D generative task assessments. Following prior work [57,

89, 96, 103], we train on three categories: *airplane*, *chair*, and *car*. We follow the dataset splits and preprocessing established in PointFlow [96]. Unless stated otherwise, each point cloud consists of 2048 points for each shape.

5.2 Evaluation metrics

In line with previous works [57, 89, 96, 103], we employ 1-nearest neighbor (1-NNA) [56], computed using both Chamfer distance (CD) and earth mover distance (EMD). 1-NNA assesses the similarity between two 3D shape distributions, considering both diversity and quality [96]. Section 6 in the supplementary provides further comparisons with two other metrics: minimum matching distance (MMD) [1] and coverage (COV) [1].

5.3 Results

Point cloud generation In Tab. 1, we benchmark our model, FrePolad, against several recent works. Demonstrating high generation fidelity and diversity, our model consistently surpasses most baselines and approaches the ground truth (training set). Importantly, FrePolad attains excellent results comparable to the state-of-the-art model LION [89] despite a simpler architecture that is computationally efficient during both training and inference (see the efficiency evaluation below). Further, by modeling each point cloud as a point distribution over a shape latent, our method facilitates sampling point clouds with arbitrary cardinality – a feature rarely available in other baselines. Figure 5 illustrates the generation with different numbers of points.

Figure 4 provides qualitative comparisons, highlighting the visually appealing and diverse point clouds generated by FrePolad across three distinct classes.

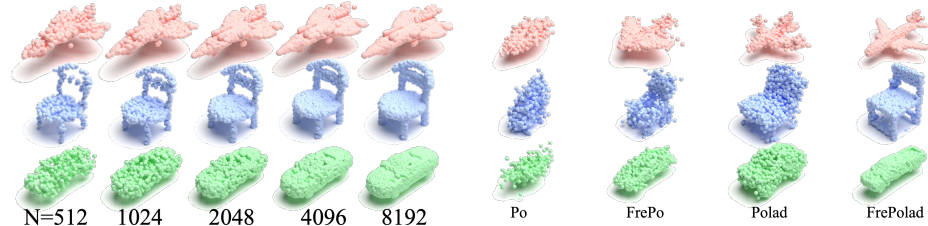


Fig. 5: FrePolad supports flexibility in the cardinality of generated point clouds.

Fig. 6: Ablation study: shape generation by three simplified versions of FrePolad.

Latent interpolation Fig. 7 showcases latent interpolations facilitated by FrePolad. The smooth transitions in the interpolated shapes suggest that our network successfully captures an effective latent space of the underlying shapes.

Model	Airplane		Chair		Car	
	CD	EMD	CD	EMD	CD	EMD
Training set	64.44	64.07	51.28	54.76	51.70	50.00
r-GAN [1]	98.40	96.79	83.69	99.70	94.46	99.01
1-GAN/CD [1]	87.30	93.95	68.58	83.84	66.49	88.78
1-GAN/EMD [1]	89.49	76.91	71.90	64.65	71.16	66.19
PointFlow [96]	75.68	70.74	62.84	60.57	58.10	56.25
SoftFlow [37]	76.05	65.80	59.21	60.05	64.77	60.09
SetVAE [39]	76.54	67.65	58.84	60.57	59.94	59.94
ShapeGF [5]	81.23	80.86	58.01	61.25	61.79	57.24
DPF-Net [44]	75.18	65.55	62.00	58.53	62.35	54.48
DPC [57]	76.42	86.91	60.05	74.77	68.89	79.97
PVD [103]	73.82	64.81	56.26	53.32	54.55	53.83
LION [89]	67.41	61.23	53.70	52.34	53.41	51.14
FrePolad (ours)	65.25	62.10	52.35	53.23	51.89	50.26

Table 1: 1-NNA scores (\downarrow) on point cloud generation on three classes of ShapeNet dataset. FrePolad achieves significant improvement over most existing models and obtains state-of-the-art results with simpler and more flexible structure.

Ablation study In Tab. 2 and Fig. 6 we also include quantitative and qualitative comparisons of three simplified variants of FrePolad. We selectively omit some components such as the frequency rectification and/or the latent DDPM:

- Polad (FrePolad without **frequency rectification**): in the first stage of training, the VAE is trained with the standard ELBO Eq. (1) in lieu of the FreELBO Eq. (15);
- FrePo (FrePolad without **latent diffusion**): instead of using a latent diffusion as the latent distribution of VAE, we assume the prior is a standard Gaussian; and
- Po (FrePolad without both).

Our results indicate that incorporating frequency rectification and latent DDPM substantially enhances the quality and diversity of the generated point clouds.

Model	Airplane		Chair		Car	
	CD	EMD	CD	EMD	CD	EMD
Po	85.93	85.94	94.53	99.22	100.0	100.0
FrePo	80.38	80.38	89.06	82.19	89.22	84.53
Polad	69.26	65.26	57.35	61.52	58.12	56.13
FrePolad	65.25	62.10	52.35	53.23	51.89	50.26

Table 2: Ablation study: 1-NNA scores (\downarrow) of three simplified versions of FrePolad. The frequency rectification and the latent DDPM bring significant improvement.

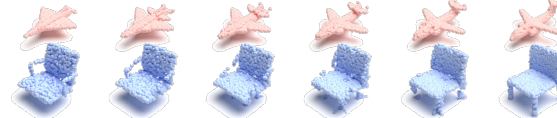


Fig. 7: Interpolation of shapes in the VAE latent space.

Computational efficiency We compare the computational efficiency of different models trained on ShapeNet airplane dataset [7]. In Tab. 3 and Fig. 1 (b) to (e), we document the computational overhead incurred by different methods during training and generation. From these results, it is evident that FrePolad exhibits a favorable computational efficiency. In contrast, considering other latent-based models, PointFlow [96] is much slower during training, likely due to its two flows (for the prior and decoder) trained jointly, whereas FrePolad only has a single flow for the decoder and we separate the training into two stages. LION [89] has a hierarchical latent space with a dimensionality larger than that of the original point cloud, leading to excessive computational cost during both training and sampling. During generation, FrePolad also achieves scalability while maintaining high quality. FrePolad’s generation time remains constant as the bulk of time is spent on the latent diffusion model, unaffected by varying output point numbers due to the consistent latent dimension. The difference becomes even more evident when generating dense point clouds containing as many as 100k points.

Model	Train (hours)	Generation (seconds per shape)			
		2048	8192	15k	100k
PointFlow [96]	360	1.73	1.76	1.77	1.81
ShapeGF [5]	28	20.60	20.71	20.87	21.42
DPC [57]	300	27.34	110	220	1370
PVD [103]	230	200	-	-	-
LION [89]	550	30.2	-	-	-
FrePolad (ours)	20	6.30	6.32	6.35	6.41

Table 3: Training cost on the airplane dataset and generation with different point cloud cardinalities. “-” means unsupported. FrePolad incurs most efficient computational cost and can be easily scaled up to generate significantly denser point clouds.

5.4 Direct generation *vs.* upsampling

The flexibility of FrePolad enables the generation of arbitrarily dense point clouds. While such dense point clouds can also be acquired by upsampling sparse ones, we claim that FrePolad’s direct generation approach yields superior quality. To demonstrate this, we consider the generation of point clouds of different

cardinalities containing 8192, 15k, and 100k points. We consider a few baselines that generate dense point clouds by upsampling sparser ones using recent, competitive methods. Due to the GPU memory constraints, we only sample 8192 points when evaluating 1-NNA-CD. The result is summarized in Tab. 4 (further results with other data classes or metrics can be found in Tab. 7 in the supplementary). We can observe that the direct generation by FrePolad vastly outperforms the upsampling approach in terms of generation quality and runtime. This comparison clearly highlights the advantage of FrePolad’s capability to directly generate dense point clouds.

Model	1-NNA-CD (↓)			Time (min)		
	8192	15k	100k	8192	15k	100k
PU-GAN [49]	100	100	100	1.17	2.44	7.55
PU-GCN [70]	100	100	100	0.83	6.67	96
Grad-PU [29]	100	100	100	0.87	2.47	68.52
FrePolad (ours)	65.31	66.87	66.25	0.11	0.11	0.11

Table 4: 1-NNA-CD (↓) and time cost of the generation of dense point clouds with different cardinalities. The first three methods upsample sparse ground truths while FrePolad directly generates dense ones. FrePolad substantially outperforms all upsampling methods in terms of generation quality and runtime, demonstrating the importance of the ability to directly generate dense point clouds.

6 Conclusion and Future Works

In this paper, we presented FrePolad, a novel method for point cloud generation. At its core, FrePolad is structured as a point cloud VAE integrated with a DDPM-based prior. To enhance sample quality and diversity, we tailor a new frequency rectification technique that preserves the high-frequency details extracted via spherical harmonics. We also incorporate a latent DDPM to model the regularized latent space of the VAE. Additionally, to achieve flexibility in the point cloud cardinality, we perceive point clouds as distributions of their constituent points over a latent shape. Our proposed model exhibits minimal training and sampling overheads and can be easily scaled to generate highly dense point clouds. Our empirical analyses, both quantitative and qualitative, showed the state-of-the-art performance achieved by FrePolad.

We currently use the standard spherical harmonic base functions $Y_{l,m}$ in Eq. (29) on the unit sphere for frequency analysis. An interesting future direction is to investigate a more general differential analysis on manifolds where the base functions are defined on the smoothed surface derived from the original point cloud. Additionally, we aspire to explore the application of frequency rectification in other domains with complex signals containing high-frequency information.

Acknowledgement

This work was supported by a UKRI Future Leaders Fellowship [grant number G104084].

References

1. Achlioptas, P., Diamanti, O., Mitliagkas, I., Guibas, L.: Learning representations and generative models for 3d point clouds. In: International conference on machine learning. pp. 40–49. PMLR (2018)
2. Blattmann, A., Rombach, R., Ling, H., Dockhorn, T., Kim, S.W., Fidler, S., Kreis, K.: Align your latents: High-resolution video synthesis with latent diffusion models. In: Proceedings of the IEEE/CVF Conference on Computer Vision and Pattern Recognition. pp. 22563–22575 (2023)
3. Bonev, B., Kurth, T., Hundt, C., Pathak, J., Baust, M., Kashinath, K., Anandkumar, A.: Spherical fourier neural operators: Learning stable dynamics on the sphere (2023)
4. Brooks, T., Holynski, A., Efros, A.A.: Instructpix2pix: Learning to follow image editing instructions. In: Proceedings of the IEEE/CVF Conference on Computer Vision and Pattern Recognition. pp. 18392–18402 (2023)
5. Cai, R., Yang, G., Averbuch-Elor, H., Hao, Z., Belongie, S., Snavely, N., Hariharan, B.: Learning gradient fields for shape generation. In: Computer Vision–ECCV 2020: 16th European Conference, Glasgow, UK, August 23–28, 2020, Proceedings, Part III 16. pp. 364–381. Springer (2020)
6. Chandrasegaran, K., Tran, N.T., Cheung, N.M.: A closer look at fourier spectrum discrepancies for cnn-generated images detection. In: Proceedings of the IEEE/CVF conference on computer vision and pattern recognition. pp. 7200–7209 (2021)
7. Chang, A.X., Funkhouser, T., Guibas, L., Hanrahan, P., Huang, Q., Li, Z., Savarese, S., Savva, M., Song, S., Su, H., et al.: Shapenet: An information-rich 3d model repository. arXiv preprint arXiv:1512.03012 (2015)
8. Chen, N., Zhang, Y., Zen, H., Weiss, R.J., Norouzi, M., Chan, W.: Wavegrad: Estimating gradients for waveform generation. arXiv preprint arXiv:2009.00713 (2020)
9. Chen, R.T., Rubanova, Y., Bettencourt, J., Duvenaud, D.K.: Neural ordinary differential equations. Advances in neural information processing systems **31** (2018)
10. Chen, X., Kingma, D.P., Salimans, T., Duan, Y., Dhariwal, P., Schulman, J., Sutskever, I., Abbeel, P.: Variational lossy autoencoder. arXiv preprint arXiv:1611.02731 (2016)
11. Courant, R., Hilbert, D.: Methods of mathematical physics: partial differential equations. John Wiley & Sons (2008)
12. Csiszár, I.: I-divergence geometry of probability distributions and minimization problems. The annals of probability pp. 146–158 (1975)
13. Czolbe, S., Krause, O., Cox, I., Igel, C.: A loss function for generative neural networks based on watson’s perceptual model. Advances in Neural Information Processing Systems **33**, 2051–2061 (2020)
14. Dhariwal, P., Nichol, A.: Diffusion models beat gans on image synthesis. Advances in neural information processing systems **34**, 8780–8794 (2021)

15. Dinh, L., Krueger, D., Bengio, Y.: Nice: Non-linear independent components estimation. arXiv preprint arXiv:1410.8516 (2014)
16. Dosovitskiy, A., Brox, T.: Generating images with perceptual similarity metrics based on deep networks. *Advances in neural information processing systems* **29** (2016)
17. Durall, R., Keuper, M., Keuper, J.: Watch your up-convolution: Cnn based generative deep neural networks are failing to reproduce spectral distributions. In: *Proceedings of the IEEE/CVF conference on computer vision and pattern recognition*. pp. 7890–7899 (2020)
18. Dzanic, T., Shah, K., Witherden, F.: Fourier spectrum discrepancies in deep network generated images. *Advances in neural information processing systems* **33**, 3022–3032 (2020)
19. Esser, P., Rombach, R., Ommer, B.: Taming transformers for high-resolution image synthesis. In: *Proceedings of the IEEE/CVF conference on computer vision and pattern recognition*. pp. 12873–12883 (2021)
20. Fan, H., Su, H., Guibas, L.J.: A point set generation network for 3d object reconstruction from a single image. In: *Proceedings of the IEEE conference on computer vision and pattern recognition*. pp. 605–613 (2017)
21. Fourier, J.: Mémoire sur la propagation de la chaleur dans les corps solides (extrait). *Nouveau Bulletin des Sciences, par la Société Philomathique de Paris* **1**, 112–16 (1808)
22. Gadelha, M., Wang, R., Maji, S.: Multiresolution tree networks for 3d point cloud processing. In: *Proceedings of the European Conference on Computer Vision (ECCV)*. pp. 103–118 (2018)
23. Gao, G., You, P., Pan, R., Han, S., Zhang, Y., Dai, Y., Lee, H.: Neural image compression via attentional multi-scale back projection and frequency decomposition. In: *Proceedings of the IEEE/CVF International Conference on Computer Vision*. pp. 14677–14686 (2021)
24. Geiger, A., Lenz, P., Stiller, C., Urtasun, R.: Vision meets robotics: The kitti dataset. *The International Journal of Robotics Research* **32**(11), 1231–1237 (2013)
25. Goodfellow, I., Pouget-Abadie, J., Mirza, M., Xu, B., Warde-Farley, D., Ozair, S., Courville, A., Bengio, Y.: Generative adversarial nets. *Advances in neural information processing systems* **27** (2014)
26. Grathwohl, W., Chen, R.T., Bettencourt, J., Sutskever, I., Duvenaud, D.: Ffjord: Free-form continuous dynamics for scalable reversible generative models. arXiv preprint arXiv:1810.01367 (2018)
27. Groueix, T., Fisher, M., Kim, V.G., Russell, B.C., Aubry, M.: A papier-mâché approach to learning 3d surface generation. In: *Proceedings of the IEEE conference on computer vision and pattern recognition*. pp. 216–224 (2018)
28. He, Y., Yang, T., Zhang, Y., Shan, Y., Chen, Q.: Latent video diffusion models for high-fidelity video generation with arbitrary lengths. arXiv preprint arXiv:2211.13221 (2022)
29. He, Y., Tang, D., Zhang, Y., Xue, X., Fu, Y.: Grad-pu: Arbitrary-scale point cloud upsampling via gradient descent with learned distance functions. In: *Proceedings of the IEEE/CVF Conference on Computer Vision and Pattern Recognition*. pp. 5354–5363 (2023)
30. Ho, J., Jain, A., Abbeel, P.: Denoising diffusion probabilistic models. *Advances in neural information processing systems* **33**, 6840–6851 (2020)
31. Ho, J., Saharia, C., Chan, W., Fleet, D.J., Norouzi, M., Salimans, T.: Cascaded diffusion models for high fidelity image generation. *The Journal of Machine Learning Research* **23**(1), 2249–2281 (2022)

32. Hou, X., Shen, L., Sun, K., Qiu, G.: Deep feature consistent variational autoencoder. In: 2017 IEEE winter conference on applications of computer vision (WACV). pp. 1133–1141. IEEE (2017)
33. Jeong, M., Kim, H., Cheon, S.J., Choi, B.J., Kim, N.S.: Diff-tts: A denoising diffusion model for text-to-speech. arXiv preprint arXiv:2104.01409 (2021)
34. Jiang, L., Dai, B., Wu, W., Loy, C.C.: Focal frequency loss for image reconstruction and synthesis. In: Proceedings of the IEEE/CVF International Conference on Computer Vision. pp. 13919–13929 (2021)
35. Johnson, J., Alahi, A., Fei-Fei, L.: Perceptual losses for real-time style transfer and super-resolution. In: Computer Vision–ECCV 2016: 14th European Conference, Amsterdam, The Netherlands, October 11–14, 2016, Proceedings, Part II 14. pp. 694–711. Springer (2016)
36. Karush, W.: Minima of functions of several variables with inequalities as side constraints. M. Sc. Dissertation. Dept. of Mathematics, Univ. of Chicago (1939)
37. Kim, H., Lee, H., Kang, W.H., Lee, J.Y., Kim, N.S.: Softflow: Probabilistic framework for normalizing flow on manifolds. Advances in Neural Information Processing Systems **33**, 16388–16397 (2020)
38. Kim, J., Hua, B.S., Nguyen, T., Yeung, S.K.: Pointinverter: Point cloud reconstruction and editing via a generative model with shape priors. In: Proceedings of the IEEE/CVF Winter Conference on Applications of Computer Vision. pp. 592–601 (2023)
39. Kim, J., Yoo, J., Lee, J., Hong, S.: Setvae: Learning hierarchical composition for generative modeling of set-structured data. In: Proceedings of the IEEE/CVF Conference on Computer Vision and Pattern Recognition. pp. 15059–15068 (2021)
40. Kim, S.Y., Aberman, K., Kanazawa, N., Garg, R., Wadhwa, N., Chang, H., Karnad, N., Kim, M., Liba, O.: Zoom-to-inpaint: Image inpainting with high-frequency details. In: Proceedings of the IEEE/CVF Conference on Computer Vision and Pattern Recognition. pp. 477–487 (2022)
41. Kingma, D., Salimans, T., Poole, B., Ho, J.: Variational diffusion models. Advances in neural information processing systems **34**, 21696–21707 (2021)
42. Kingma, D.P., Welling, M.: Auto-encoding variational bayes. arXiv preprint arXiv:1312.6114 (2013)
43. Kingma, D.P., Dhariwal, P.: Glow: Generative flow with invertible 1x1 convolutions. Advances in neural information processing systems **31** (2018)
44. Klokov, R., Boyer, E., Verbeek, J.: Discrete point flow networks for efficient point cloud generation. In: European Conference on Computer Vision. pp. 694–710. Springer (2020)
45. Kuhn, H., Tucker, A.: Nonlinear programming. In: Proceedings of 2nd Berkeley symposium (pp. 481–492) (1951)
46. Kurenkov, A., Ji, J., Garg, A., Mehta, V., Gwak, J., Choy, C., Savarese, S.: Deformnet: Free-form deformation network for 3d shape reconstruction from a single image. In: 2018 IEEE Winter Conference on Applications of Computer Vision (WACV). pp. 858–866. IEEE (2018)
47. Lee, D., Kim, C., Kim, S., Cho, M., Han, W.S.: Autoregressive image generation using residual quantization. In: Proceedings of the IEEE/CVF Conference on Computer Vision and Pattern Recognition. pp. 11523–11532 (2022)
48. Li, C.L., Zaheer, M., Zhang, Y., Poczos, B., Salakhutdinov, R.: Point cloud gan. arXiv preprint arXiv:1810.05795 (2018)
49. Li, R., Li, X., Fu, C.W., Cohen-Or, D., Heng, P.A.: Pu-gan: a point cloud up-sampling adversarial network. In: Proceedings of the IEEE/CVF international conference on computer vision. pp. 7203–7212 (2019)

50. Li, S., Liu, M., Walder, C.: Editvae: Unsupervised parts-aware controllable 3d point cloud shape generation. In: Proceedings of the AAAI Conference on Artificial Intelligence. vol. 36, pp. 1386–1394 (2022)
51. Li, S., Walder, C., Liu, M.: Spa-vae: Similar-parts-assignment for unsupervised 3d point cloud generation. arXiv preprint arXiv:2203.07825 (2022)
52. Li, Y., Baciu, G.: Hsgan: Hierarchical graph learning for point cloud generation. *IEEE Transactions on Image Processing* **30**, 4540–4554 (2021)
53. Lin, X., Li, Y., Hsiao, J., Ho, C., Kong, Y.: Catch missing details: Image reconstruction with frequency augmented variational autoencoder. In: Proceedings of the IEEE/CVF Conference on Computer Vision and Pattern Recognition. pp. 1736–1745 (2023)
54. Liu, S., Su, D., Yu, D.: Diffgan-tts: High-fidelity and efficient text-to-speech with denoising diffusion gans. arXiv preprint arXiv:2201.11972 (2022)
55. Liu, Z., Tang, H., Lin, Y., Han, S.: Point-voxel cnn for efficient 3d deep learning. *Advances in Neural Information Processing Systems* **32** (2019)
56. Lopez-Paz, D., Oquab, M.: Revisiting classifier two-sample tests. arXiv preprint arXiv:1610.06545 (2016)
57. Luo, S., Hu, W.: Diffusion probabilistic models for 3d point cloud generation. In: Proceedings of the IEEE/CVF Conference on Computer Vision and Pattern Recognition. pp. 2837–2845 (2021)
58. Mildenhall, B., Srinivasan, P.P., Tancik, M., Barron, J.T., Ramamoorthi, R., Ng, R.: Nerf: Representing scenes as neural radiance fields for view synthesis. *Communications of the ACM* **65**(1), 99–106 (2021)
59. Mittal, G., Engel, J., Hawthorne, C., Simon, I.: Symbolic music generation with diffusion models. arXiv preprint arXiv:2103.16091 (2021)
60. Mo, S., Xie, E., Chu, R., Yao, L., Hong, L., Nießner, M., Li, Z.: Dit-3d: Exploring plain diffusion transformers for 3d shape generation. arXiv preprint arXiv:2307.01831 (2023)
61. Mustafa, A., Hanji, P., Mantiuk, R.: Distilling style from image pairs for global forward and inverse tone mapping. In: Proceedings of the 19th ACM SIGGRAPH European Conference on Visual Media Production. pp. 1–10 (2022)
62. Naderi, H., Noorbakhsh, K., Etemadi, A., Kasaei, S.: Lpf-defense: 3d adversarial defense based on frequency analysis. *Plos one* **18**(2), e0271388 (2023)
63. Nakayama, G.K., Uy, M.A., Huang, J., Hu, S.M., Li, K., Guibas, L.: Difffacto: Controllable part-based 3d point cloud generation with cross diffusion. In: Proceedings of the IEEE/CVF International Conference on Computer Vision. pp. 14257–14267 (2023)
64. Pandey, K., Mukherjee, A., Rai, P., Kumar, A.: Diffusevae: Efficient, controllable and high-fidelity generation from low-dimensional latents. arXiv preprint arXiv:2201.00308 (2022)
65. Piotrowski, A.P., Napiorkowski, J.J.: A comparison of methods to avoid overfitting in neural networks training in the case of catchment runoff modelling. *Journal of Hydrology* **476**, 97–111 (2013)
66. Poole, B., Jain, A., Barron, J.T., Mildenhall, B.: Dreamfusion: Text-to-3d using 2d diffusion. arXiv (2022)
67. Preechakul, K., Chatthee, N., Wizadwongsu, S., Suwajanakorn, S.: Diffusion autoencoders: Toward a meaningful and decodable representation. In: Proceedings of the IEEE/CVF Conference on Computer Vision and Pattern Recognition. pp. 10619–10629 (2022)

68. Qi, C.R., Su, H., Mo, K., Guibas, L.J.: Pointnet: Deep learning on point sets for 3d classification and segmentation. In: Proceedings of the IEEE conference on computer vision and pattern recognition. pp. 652–660 (2017)
69. Qi, C.R., Yi, L., Su, H., Guibas, L.J.: Pointnet++: Deep hierarchical feature learning on point sets in a metric space. Advances in neural information processing systems **30** (2017)
70. Qian, G., Abualshour, A., Li, G., Thabet, A., Ghanem, B.: Pu-gcn: Point cloud upsampling using graph convolutional networks. In: Proceedings of the IEEE/CVF Conference on Computer Vision and Pattern Recognition (CVPR). pp. 11683–11692 (June 2021)
71. Rahaman, N., Baratin, A., Arpit, D., Draxler, F., Lin, M., Hamprecht, F., Bengio, Y., Courville, A.: On the spectral bias of neural networks. In: International Conference on Machine Learning. pp. 5301–5310. PMLR (2019)
72. Rahimi, A., Recht, B.: Random features for large-scale kernel machines. Advances in neural information processing systems **20** (2007)
73. Ramesh, A., Dhariwal, P., Nichol, A., Chu, C., Chen, M.: Hierarchical text-conditional image generation with clip latents. arXiv preprint arXiv:2204.06125 **1**(2), 3 (2022)
74. Razavi, A., Van den Oord, A., Vinyals, O.: Generating diverse high-fidelity images with vq-vae-2. Advances in neural information processing systems **32** (2019)
75. Rezende, D., Mohamed, S.: Variational inference with normalizing flows. In: International conference on machine learning. pp. 1530–1538. PMLR (2015)
76. Rezende, D.J., Mohamed, S., Wierstra, D.: Stochastic backpropagation and approximate inference in deep generative models. In: International conference on machine learning. pp. 1278–1286. PMLR (2014)
77. Rombach, R., Blattmann, A., Lorenz, D., Esser, P., Ommer, B.: High-resolution image synthesis with latent diffusion models. In: Proceedings of the IEEE/CVF Conference on Computer Vision and Pattern Recognition. pp. 10684–10695 (2022)
78. Ronneberger, O., Fischer, P., Brox, T.: U-net: Convolutional networks for biomedical image segmentation. In: Medical Image Computing and Computer-Assisted Intervention–MICCAI 2015: 18th International Conference, Munich, Germany, October 5–9, 2015, Proceedings, Part III 18. pp. 234–241. Springer (2015)
79. Rosca, M., Lakshminarayanan, B., Mohamed, S.: Distribution matching in variational inference. arXiv preprint arXiv:1802.06847 (2018)
80. Serna, A., Marcotegui, B., Goulette, F., Deschaud, J.E.: Paris-rue-madame database: a 3d mobile laser scanner dataset for benchmarking urban detection, segmentation and classification methods. In: 4th international conference on pattern recognition, applications and methods ICPRAM 2014 (2014)
81. Shu, D.W., Park, S.W., Kwon, J.: 3d point cloud generative adversarial network based on tree structured graph convolutions. In: Proceedings of the IEEE/CVF international conference on computer vision. pp. 3859–3868 (2019)
82. Sinha, A., Song, J., Meng, C., Ermon, S.: D2c: Diffusion-decoding models for few-shot conditional generation. Advances in Neural Information Processing Systems **34**, 12533–12548 (2021)
83. Sohl-Dickstein, J., Weiss, E., Maheswaranathan, N., Ganguli, S.: Deep unsupervised learning using nonequilibrium thermodynamics. In: International conference on machine learning. pp. 2256–2265. PMLR (2015)
84. Song, Y., Shen, L., Xing, L., Ermon, S.: Solving inverse problems in medical imaging with score-based generative models. arXiv preprint arXiv:2111.08005 (2021)

85. Sun, Y., Wang, Y., Liu, Z., Siegel, J., Sarma, S.: Pointgrow: Autoregressively learned point cloud generation with self-attention. In: Proceedings of the IEEE/CVF Winter Conference on Applications of Computer Vision. pp. 61–70 (2020)
86. Tancik, M., Srinivasan, P., Mildenhall, B., Fridovich-Keil, S., Raghavan, N., Singhal, U., Ramamoorthi, R., Barron, J., Ng, R.: Fourier features let networks learn high frequency functions in low dimensional domains. Advances in Neural Information Processing Systems **33**, 7537–7547 (2020)
87. Tomczak, J., Welling, M.: Vae with a vampprior. In: International Conference on Artificial Intelligence and Statistics. pp. 1214–1223. PMLR (2018)
88. Vahdat, A., Kreis, K., Kautz, J.: Score-based generative modeling in latent space. Advances in Neural Information Processing Systems **34**, 11287–11302 (2021)
89. Vahdat, A., Williams, F., Gojcic, Z., Litany, O., Fidler, S., Kreis, K., et al.: Lion: Latent point diffusion models for 3d shape generation. Advances in Neural Information Processing Systems **35**, 10021–10039 (2022)
90. Vaswani, A., Shazeer, N., Parmar, N., Uszkoreit, J., Jones, L., Gomez, A.N., Kaiser, Ł., Polosukhin, I.: Attention is all you need. Advances in neural information processing systems **30** (2017)
91. Wang, L., Huang, Y., Tao, P., Hou, Y., Liu, Y.: Learning geometry-image representation for 3d point cloud generation. arXiv preprint arXiv:2011.14289 (2020)
92. Wang, Y., Cai, L., Zhang, D., Huang, S.: The frequency discrepancy between real and generated images. IEEE Access **9**, 115205–115216 (2021)
93. Whang, J., Lindgren, E., Dimakis, A.: Composing normalizing flows for inverse problems. In: International Conference on Machine Learning. pp. 11158–11169. PMLR (2021)
94. Wu, L., Wang, D., Gong, C., Liu, X., Xiong, Y., Ranjan, R., Krishnamoorthi, R., Chandra, V., Liu, Q.: Fast point cloud generation with straight flows. In: Proceedings of the IEEE/CVF Conference on Computer Vision and Pattern Recognition. pp. 9445–9454 (2023)
95. Xu, Z.Q.J., Zhang, Y., Luo, T., Xiao, Y., Ma, Z.: Frequency principle: Fourier analysis sheds light on deep neural networks. arXiv preprint arXiv:1901.06523 (2019)
96. Yang, G., Huang, X., Hao, Z., Liu, M.Y., Belongie, S., Hariharan, B.: Pointflow: 3d point cloud generation with continuous normalizing flows. In: Proceedings of the IEEE/CVF international conference on computer vision. pp. 4541–4550 (2019)
97. Yang, Y., Feng, C., Shen, Y., Tian, D.: Foldingnet: Point cloud auto-encoder via deep grid deformation. In: Proceedings of the IEEE conference on computer vision and pattern recognition. pp. 206–215 (2018)
98. Yu, L., Li, X., Fu, C.W., Cohen-Or, D., Heng, P.A.: Ec-net: an edge-aware point set consolidation network. In: Proceedings of the European conference on computer vision (ECCV). pp. 386–402 (2018)
99. Zamorski, M., Zięba, M., Klukowski, P., Nowak, R., Kurach, K., Stokowiec, W., Trzciński, T.: Adversarial autoencoders for compact representations of 3d point clouds. Computer Vision and Image Understanding **193**, 102921 (2020)
100. Zhang, R., Chen, J., Gao, W., Li, G., Li, T.H.: Pointot: Interpretable geometry-inspired point cloud generative model via optimal transport. IEEE Transactions on Circuits and Systems for Video Technology **32**(10), 6792–6806 (2022)
101. Zhang, Y., Tiño, P., Leonardis, A., Tang, K.: A survey on neural network interpretability. IEEE Transactions on Emerging Topics in Computational Intelligence **5**(5), 726–742 (2021)

102. Zhou, D., Wang, W., Yan, H., Lv, W., Zhu, Y., Feng, J.: Magicvideo: Efficient video generation with latent diffusion models. arXiv preprint arXiv:2211.11018 (2022)
103. Zhou, L., Du, Y., Wu, J.: 3d shape generation and completion through point-voxel diffusion. In: Proceedings of the IEEE/CVF International Conference on Computer Vision. pp. 5826–5835 (2021)

FrePolad: Frequency-Rectified Point Latent Diffusion for Point Cloud Generation

Supplementary Material

Denoising Diffusion Probabilistic Model

Given a data sample $\mathbf{z} \sim q(\mathbf{z})$, at each time step $t = 1, 2, \dots, T$, DDPMs [30, 83] gradually transform $\mathbf{z} = \mathbf{z}_0$ into \mathbf{z}_T by adding noise in a Markovian *diffusion process* defined by

$$q(\mathbf{z}_{1:T}|\mathbf{z}_0) := \prod_{t=1}^T q(\mathbf{z}_t|\mathbf{z}_{t-1}); \quad (18)$$

$$q(\mathbf{z}_t|\mathbf{z}_{t-1}) := \mathcal{N}\left(\sqrt{1-\beta_t}\mathbf{z}_{t-1}, \beta_t I\right), \quad (19)$$

where $\mathcal{N}(\boldsymbol{\mu}, \boldsymbol{\sigma})$ denotes multivariate Gaussian distribution with mean $\boldsymbol{\mu}$ and variance $\boldsymbol{\sigma}$, and $\{\beta_t\}_t$ is a pre-determined variance schedule controlling the rate of diffusion. If T is sufficiently large (1000 steps in practice), $p(\mathbf{z}_T)$ approaches the standard Gaussian.

DDPMs learn an inverse Markovian process called *reverse process* parametrized by ζ that inverts the forward diffusion, transforming the standard Gaussian noise \mathbf{z}_T back to a data sample:

$$p_\zeta(\mathbf{z}_{0:T}) := p(\mathbf{z}_T) \prod_{t=1}^T p_\zeta(\mathbf{z}_{t-1}|\mathbf{z}_t); \quad (20)$$

$$p_\zeta(\mathbf{z}_{t-1}|\mathbf{z}_t) := \mathcal{N}\left(\mu_\zeta(\mathbf{z}_t, t), \sigma_t^2 I\right), \quad (21)$$

where $\mu_\zeta(\mathbf{z}_t, t)$ represents the predicted mean for the Gaussian distribution at time step t and $\{\sigma_t\}_t$ is the variance schedule.

DDPMs are trained by maximizing the variational lower bound of log-likelihood of the data \mathbf{z}_0 under $q(\mathbf{z}_0)$:

$$\mathbb{E}_{q(\mathbf{z}_0)} [\log p_\zeta(\mathbf{z}_0)] \geq \mathbb{E}_{q(\mathbf{z}_{0:T})} \left[\log \frac{p_\zeta(\mathbf{z}_{0:T})}{q(\mathbf{z}_{1:T}|\mathbf{z}_0)} \right]. \quad (22)$$

Expanding Eq. (22) with Eq. (20) and noticing that $p(\mathbf{z}_T)$ and $q(\mathbf{z}_{1:T}|\mathbf{z}_0)$ are constant with respect to ζ , we obtain our objective function to maximize:

$$\mathbb{E}_{q(\mathbf{z}_0), q(\mathbf{z}_{1:T}|\mathbf{z}_0)} \left[\sum_{t=1}^T \log p_\zeta(\mathbf{z}_{t-1}|\mathbf{z}_t) \right]. \quad (23)$$

Since we can factor the joint posterior

$$q(\mathbf{z}_{1:T}|\mathbf{z}_0) = \prod_{t=1}^T q(\mathbf{z}_{t-1}|\mathbf{z}_t, \mathbf{z}_0) \quad (24)$$

and both $q(\mathbf{z}_{t-1}|\mathbf{z}_t, \mathbf{z}_0)$ and $p_\zeta(\mathbf{z}_{t-1}|\mathbf{z}_t)$ are Gaussian, maximizing Eq. (23) can be reduced to minimizing the following loss:

$$\mathcal{L}_{\text{DDPM}}(\zeta) := \mathbb{E}_{q(\mathbf{z}_0), t \sim \mathcal{U}(1, T), \epsilon \sim \mathcal{N}(0, I)} [\|\epsilon - \epsilon_\zeta(\mathbf{z}_t, t)\|_2^2], \quad (25)$$

where $\mathcal{U}(1, T)$ is the uniform distribution on $\{1, 2, \dots, T\}$. Note that here we employ a commonly used parametrization

$$\mu_\zeta(\mathbf{z}_t, t) = \frac{1}{\sqrt{1 - \beta_t}} \left(\mathbf{z}_t - \frac{\beta_t}{\gamma_t} \epsilon_\zeta(\mathbf{z}_t, t) \right) \quad (26)$$

and that via Eq. (19) \mathbf{z}_t is in fact tractable from the initial \mathbf{z}_0 by

$$\mathbf{z}_t = \alpha_t \mathbf{z}_0 + \gamma_t \epsilon, \quad (27)$$

where $\alpha_t := \prod_{i=1}^t \sqrt{1 - \beta_i}$ and $\gamma_t := \sqrt{1 - \alpha_t^2}$. Intuitively, minimizing the loss Eq. (25) amounts to predict the noise ϵ necessary to denoise the diffused sample \mathbf{z}_t .

During inference time, DDPMs can be iteratively sampled with ancestral sampling by first sampling \mathbf{z}_T from $p(\mathbf{z}_T) := \mathcal{N}(0, I)$ and following Eq. (21); that is:

$$p_\zeta(\mathbf{z}) = p(\mathbf{z}_T) p_\zeta(\mathbf{z}|\mathbf{z}_T) = p(\mathbf{z}_T) \prod_{t=1}^T p_\zeta(\mathbf{z}_{t-1}|\mathbf{z}_t) \quad (28)$$

for $p(\mathbf{z}_T) := \mathcal{N}(0, I)$.

Spherical Harmonics

The spherical harmonics [11] are a set of complex-valued spherical harmonic base functions $Y_{l,m} : S^2 \rightarrow \mathbb{C}$ defined on a unit sphere S^2 , indexed by the degree $l \geq 0$ and order m ($-l \leq m \leq l$):

$$Y_{l,m}(\theta, \varphi) := Z_{l,m} e^{im\varphi} P_{l,m}(\cos \theta), \quad (29)$$

where the colatitude $\theta \in [0, \pi]$, the longitude $\varphi \in [0, 2\pi]$, $Z_{l,m} \in \mathbb{C}$ is the normalization constant, i is the imaginary unit, and $P_{l,m} : [-1, 1] \rightarrow \mathbb{R}$ is the associated Legendre polynomial of degree l and order m satisfying the general Legendre equation:

$$\frac{d}{dx} \left[(1 - x^2) \frac{d}{dx} P_{l,m}(x) \right] + \left[l(l+1) - \frac{m^2}{1 - x^2} \right] P_{l,m}(x) = 0. \quad (30)$$

Note that for a fixed degree l , any $Y_{l,m}$ for $-l \leq m \leq l$ are solutions to the differential equation

$$\Delta Y_{l,m} = -l(l+1)Y_{l,m}, \quad (31)$$

where Δ is the Laplace operator, and that every solution to Eq. (31) is a linear combination of $Y_{l,m}$, $-l \leq m \leq l$. In other words, spherical harmonics base

functions are eigenfunctions of the Laplace operator (or, more generally in higher dimensions, the Laplace-Beltrami operator).

The spherical harmonics are a complete set of orthonormal functions and thus form an orthonormal basis for square-integrable functions defined on the unit sphere $L^2(S^2)$ [71]; *i.e.*, every continuous function $f : S^2 \rightarrow \mathbb{C}$ such that

$$\int_0^{2\pi} \int_0^\pi |f(\theta, \varphi)|^2 d\theta d\varphi < \infty \quad (32)$$

can be represented as a series of these spherical harmonic base functions $Y_{l,m}$ by

$$f(\theta, \varphi) = \sum_{l=0}^{\infty} \sum_{m=-l}^l c_{l,m} Y_{l,m}(\theta, \varphi), \quad (33)$$

where the coefficients $c_{l,m}$ can be calculated by

$$c_{l,m} = \int_0^{2\pi} \int_0^\pi f(\theta, \varphi) \overline{Y_{l,m}(\theta, \varphi)} \sin(\theta) d\theta d\varphi. \quad (34)$$

This is parallel to the result from Fourier analysis [21] that any arbitrary function defined on a plane can be expressed as a trigonometric series. The trigonometric functions in a Fourier series capture the fundamental modes of vibration on a plane whereas the spherical harmonics denote these modes of vibration on a sphere. Consequently, spherical harmonics cast spatial data into the spectral domain, allowing the extraction of frequency-specific information: coefficients $c_{l,m}$ with a higher degree measure the intensity of the original data in a higher-frequency domain. Please refer to Sec. 6 in the supplementary for more details about spherical harmonics.

Continuous Normalizing Flow

Normalizing flows [75] consist of a sequence of reversible mappings $\{g^i\}_{i=1}^n$. It assumes that the data points $\mathbf{x} = \mathbf{x}_n$ are obtained by iteratively transforming a sample from an initial distribution $p(\mathbf{x}_0)$:

$$\mathbf{x}_n := (g^n \circ g^{n-1} \circ \cdots \circ g^1)(\mathbf{x}_0). \quad (35)$$

The probability density of the resultant variable \mathbf{x}_n can be determined using the change of variables formula:

$$\log p(\mathbf{x}_n) = \log p(\mathbf{x}_0) - \sum_{i=1}^n \log \left| \det \left(\frac{\partial g^i(\mathbf{x}_{i-1})}{\partial \mathbf{x}_{i-1}} \right) \right|, \quad (36)$$

where \mathbf{x}_0 can be computed from \mathbf{x}_n using the inverse flow

$$\mathbf{x}_0 = (g^1 \circ \cdots \circ g^{n-1} \circ g^n)(\mathbf{x}_n), \quad (37)$$

and $\det(\cdot)$ is the Jacobian determinant function.

In practice, the initial distribution $p(\mathbf{x}_0)$ is chosen to be the standard Gaussian $\mathcal{N}(0, I)$, and the invertible mappings $\{g^i\}_{i=1}^n$ are represented by neural networks $\{g_\xi^i\}_{i=1}^n$ parameterized by ξ for which the Jacobian determinant $\left|\det\left(\frac{\partial g_\xi^i(\mathbf{x}_{i-1})}{\partial \mathbf{x}_{i-1}}\right)\right|$ is easy to compute. Since the exact log-likelihood of input data is tractable via Eq. (36), the training of normalizing flows just involves maximizing Eq. (36).

Normalizing flows can be generalized to continuous normalizing flows (CNFs) [9, 26], where a sequence of mappings $\{g_\xi(\cdot, t)\}_{t=0}^\tau$ indexed by a real number $t \in \mathbb{R}$ transforms an initial point $\mathbf{x}(0) \sim p(\mathbf{x}_0)$ into $\mathbf{x}(\tau)$ following a continuous-time dynamic

$$\frac{\partial \mathbf{x}_t}{\partial t} = g_\xi(\mathbf{x}(t), t), \quad (38)$$

and therefore

$$\mathbf{x}(\tau) = \mathbf{x}(0) + \int_0^\tau g_\xi(\mathbf{x}(0), t) dt. \quad (39)$$

Under this formulation, the probability density function $p(\mathbf{x}(\tau))$ of the transformed variable $\mathbf{x}(\tau)$ can be determined via

$$\log p(\mathbf{x}(\tau)) = \log p(\mathbf{x}(0)) - \int_0^\tau \text{Tr}\left(\frac{\partial g_\xi(\mathbf{x}(t), t)}{\partial \mathbf{x}(t)}\right), \quad (40)$$

where $\mathbf{x}(0)$ can be computed from $\mathbf{x}(\tau)$ by

$$\mathbf{x}(0) = \mathbf{x}(\tau) - \int_0^\tau g_\xi(\mathbf{x}(0), t) dt, \quad (41)$$

and $\text{Tr}(\cdot)$ is the trace function. Similarly, the training of CNFs amounts to maximizing the data log-likelihood Eq. (40).

CNFs can be further extended to be conditioned on a vector \mathbf{z} by using $g_\xi(\cdot, t, \mathbf{z})$ in place of $g_\xi(\cdot, t)$. This allows to compute the conditional probability of the data conditioned on \mathbf{z} :

$$\log p(\mathbf{x}(\tau)|\mathbf{z}) = \log p(\mathbf{x}(0)) - \int_0^\tau \text{Tr}\left(\frac{\partial g_\xi(\mathbf{x}(t), t, \mathbf{z})}{\partial \mathbf{x}(t)}\right); \quad (42)$$

$$\mathbf{x}(0) = \mathbf{x}(\tau) - \int_0^\tau g_\xi(\mathbf{x}(0), t, \mathbf{z}) dt. \quad (43)$$

To sample a CNF, we first sample an initial point $\mathbf{x}(0) \sim p(\mathbf{x}_0)$, then simply follow Eq. (39).

Training Details

In all experiments we set the latent dimension $D_z = 1024$, the number of closest neighbors to consider $k = 5$ in Eq. (7), $\sigma_{\text{KNN}} = 0.05$ in Eq. (9), the KKT multiplier (or the coefficient for the high-frequency reconstruction loss) $\eta = 5 \times 10^6$ in Eq. (15), and the maximum degree $L = 50$ and $\sigma_{\text{Fre}} = 50$ in Eq. (11).

We did a grid search to setup these hyperparameter values. Specifically, σ_{KNN} candidates were set at 0.001, 0.01, 0.05, and 0.1, and σ_{Fre} at 1, 10, 50, 100. The rationale for a smaller σ_{KNN} is to limit the influence of distant points in constructing the representative function for a point cloud. Conversely, a larger σ_{Fre} is preferred to take into account the reconstruction of both high- and low-frequency data. Additionally, L values of 25, 50, 75, and 100 were tested; higher L values enhance frequency domain partition accuracy but increase computational demands. The choice of $L = 50$ aligns with common practice in spherical harmonics examples.

We use an Adam optimizer with an initial learning rate of 10^{-3} for VAE training and 10^{-5} for latent DDPM training with $\beta_1 = 0.9$ and $\beta_2 = 0.999$. We use a weight decay of 10^{-8} . During training, the learning rate is decayed by a factor of 10 whenever the loss plateaus for more than five epochs.

We utilized the Python library `torch_harmonics` [3] for differentiable computation of coefficients as per Eq. (6).

We run all experiments on a machine with a single GPU Nvidia GeForce RTX 4090. Where relevant, all DDPMs are sampled using 1000 time steps.

Further Quantitative Comparisons

We present further quantitative comparisons of different models on point cloud generation task by considering more metrics and more ShapeNet data classes. We employ three evaluative scores for generative models: minimum matching distance (MMD) [1], coverage (COV) [1], and 1-nearest neighbor (1-NNA) [56]. Each score can be computed using Chamfer distance (CD) or earth mover distance (EMD), totaling six metrics. While MMD gauges generation fidelity, it remains insensitive to suboptimal samples. Conversely, COV quantifies generation diversity, and 1-NNA measures the distributional similarity between two sets of point clouds, taking both diversity and quality into account. More detailed discussion regarding these metrics can be found in [96].

Table 5 is the full version of Tab. 1 for quantitative comparison of point cloud generation task on three classes of ShapeNet dataset. Table 6 is the full version of Tab. 2 for FrePolad’s ablation study. Table 7 is the full version of Tab. 4 comparing the performance of FrePolad’s direct generation of dense point clouds against generation via upsampling from sparse point clouds using various upsampling methods.

Class	Model	MMD \downarrow		COV (%) \uparrow		1-NNA (%) \downarrow	
		CD	EMD	CD	EMD	CD	EMD
	Training set	0.218	0.373	46.91	52.10	64.44	64.07
	r-GAN [1]	0.447	2.309	30.12	14.32	98.40	96.79
	1-GAN (CD) [1]	0.340	0.583	38.52	21.23	87.30	93.95
	1-GAN (EMD) [1]	0.397	0.417	38.27	38.52	89.49	76.91
	PointFlow [96]	0.224	0.390	47.90	46.41	75.68	70.74
Airplane	SoftFlow [37]	0.231	0.375	46.91	47.90	76.05	65.80
	SetVAE [39]	0.200	0.367	43.70	48.40	76.54	67.65
	ShapeGF [5]	0.313	0.637	45.19	40.25	81.23	80.86
	DPF-Net [44]	0.264	0.409	46.17	48.89	75.18	65.55
	DPC [57]	0.213	0.572	48.64	33.83	76.42	86.91
	PVD [103]	0.224	0.370	48.88	52.09	73.82	64.81
	LION [89]	0.219	0.372	47.16	49.63	67.41	61.23
	FrePolad (ours)	0.204	0.353	45.16	47.80	65.25	62.10
	Training set	2.618	1.555	53.02	51.21	51.28	54.76
	r-GAN [1]	5.151	8.312	24.27	15.13	83.69	99.70
	1-GAN (CD) [1]	2.589	2.007	41.99	29.31	68.58	83.84
	1-GAN (EMD) [1]	2.811	1.619	38.07	44.86	71.90	64.65
	PointFlow [96]	2.409	1.595	42.90	50.00	62.84	60.57
Chair	SoftFlow [37]	2.528	1.682	41.39	47.43	59.21	60.05
	SetVAE [39]	2.545	1.585	46.83	44.26	58.84	60.57
	ShapeGF [5]	3.724	2.394	48.34	44.26	58.01	61.25
	DPF-Net [44]	2.536	1.632	44.71	48.79	62.00	58.53
	DPC [57]	2.399	2.066	44.86	35.50	60.05	74.77
	PVD [103]	2.622	1.556	49.84	50.60	56.26	53.32
	LION [89]	2.640	1.550	48.94	52.11	53.70	52.34
	FrePolad (ours)	2.542	1.532	50.28	50.93	52.35	53.23
	Training set	0.938	0.791	50.85	55.68	51.70	50.00
	r-GAN [1]	1.446	2.133	19.03	6.539	94.46	99.01
	1-GAN (CD) [1]	1.532	1.226	38.92	23.58	66.49	88.78
	1-GAN (EMD) [1]	1.408	0.899	37.78	45.17	71.16	66.19
	PointFlow [96]	0.901	0.807	46.88	50.00	58.10	56.25
Car	SoftFlow [37]	1.187	0.859	42.90	44.60	64.77	60.09
	SetVAE [39]	0.882	0.733	49.15	46.59	59.94	59.94
	ShapeGF [5]	1.020	0.824	44.03	47.19	61.79	57.24
	DPF-Net [44]	1.129	0.853	45.74	49.43	62.35	54.48
	DPC [57]	0.902	1.140	44.03	34.94	68.89	79.97
	PVD [103]	1.007	0.794	41.19	50.56	54.55	53.83
	LION [89]	0.913	0.752	50.00	56.53	53.41	51.14
	FrePolad (ours)	0.904	0.782	50.14	55.23	51.89	50.26

Table 5: Quantitative comparison of point cloud generation on three classes of ShapeNet dataset. MMD-CD is multiplied by 10^3 and MMD-EMD is multiplied by 10^2 . FrePolad achieves significant improvement over most existing models and obtains state-of-the-art results with simpler and more flexible structure.

Class	Model	MMD \downarrow		COV (%) \uparrow		1-NNA (%) \downarrow	
		CD	EMD	CD	EMD	CD	EMD
	Training set	0.218	0.373	46.91	52.10	64.44	64.07
Airplane	Po	0.871	0.804	23.44	35.06	85.93	85.94
	FrePo	0.757	0.730	26.56	40.38	80.38	80.38
	Polad	0.279	0.383	45.12	47.96	69.26	65.26
	FrePolad	0.204	0.353	45.16	47.80	65.25	62.10
	Training set	2.618	1.555	53.02	51.21	51.28	54.76
Chair	Po	5.253	3.393	17.19	14.06	94.53	99.22
	FrePo	5.160	2.498	24.06	27.19	89.06	82.19
	Polad	2.721	1.642	48.23	47.73	57.35	61.52
	FrePolad	2.542	1.532	50.28	50.93	52.35	53.23
	Training set	0.938	0.791	50.85	55.68	51.70	50.00
Car	Po	1.866	11.24	18.75	9.375	100.0	100.0
	FrePo	1.011	2.057	27.81	28.75	89.22	84.53
	Polad	1.148	0.817	46.23	49.10	58.12	56.13
	FrePolad	0.904	0.782	50.14	55.23	51.89	50.26

Table 6: Ablation study: quantitative comparison of three weakened versions of FrePolad: Polad (without frequency rectification), FrePo (without latent diffusion), and Po (without either). MMD-CD is multiplied by 10^3 and MMD-EMD is multiplied by 10^2 . The frequency rectification and the latent DDPM bring significant improvement to FrePolad.

Class	Model	8192		15k		100k	
		CD	EMD	CD	EMD	CD	EMD
Airplane	PU-GAN [49]	100	99.38	100	99.06	100	99.06
	PU-GCN [70]	100	99.38	100	99.38	100	99.38
	Grad-PU [29]	100	99.38	100	99.38	100	99.38
	FrePolad (ours)	65.31	63.88	66.87	57.81	66.25	60.25
Chair	PU-GAN [49]	100	100	100	100	100	100
	PU-GCN [70]	100	100	100	100	100	100
	Grad-PU [29]	100	100	100	100	100	100
	FrePolad (ours)	52.69	50.63	53.63	50.00	52.69	51.56
Car	PU-GAN [49]	99.06	98.75	99.06	98.75	99.06	98.13
	PU-GCN [70]	99.38	99.06	99.38	99.06	99.38	99.06
	Grad-PU [29]	99.38	98.75	99.38	98.75	99.38	98.75
	FrePolad (ours)	52.06	54.25	52.06	51.75	51.13	51.50

Table 7: 1-NNA scores (\downarrow) of the generated dense point clouds with different cardinalities. FrePolad directly generates dense point clouds. The first three methods upsample sparse ground truth ones. FrePolad profoundly outperforms all upsampling methods, demonstrating the importance of the ability to directly generate dense point clouds.